applied sciences

MDPI

Article

High-Precision Isogeometric Static Bending Analysis of Functionally Graded Plates Using a New Quasi-3D Spectral Displacement Formulation

Shaowei Yang, Xianbo Sun, Zhiqin Cai *, Haijun Peng and Yahui Zhang

Department of Engineering Mechanics, Dalian University of Technology, Dalian 116023, China; qinchao98998@gmail.com (S.Y.); 21303083@mail.dlut.edu.cn (X.S.); hjpeng@dlut.edu.cn (H.P.); zhangyh@dlut.edu.cn (Y.Z.)
* Correspondence: zhqcai@dlut.edu.cn; Tel.: +86-41-18470-8390

Featured Application: A new quasi-3D shear deformation theory is proposed for static bending analyses of functionally graded plates. This work can provide fundamental support for the comprehensive design and analysis of functionally graded plates.

Abstract: A new quasi-three-dimensional (3D) shear deformation theory, called the spectral displacement formulation (SDF), is proposed for high-precision static bending analyses of functionally graded plates. The main idea is to expand unknown displacement fields into Chebyshev series of a unique form in the thickness direction; the truncation numbers are set to be adjustable to meet various application requirements. Specifically, 3D elasticity solutions and traction-free boundary conditions can be approached by increasing the number of Chebyshev bases. The SDF is also an extension of the classical plate theory and naturally avoids the shear locking problem, making it versatile for functionally graded material (FGM) plates of arbitrary thicknesses. The C1 continuity requirement for the discretization of the generalized displacements is conveniently fulfilled by the nonuniform rational B-splines (NURBS)-based isogeometric method. Numerical examples demonstrate the excellent performance of the proposed method for the displacement and stress analyses of functionally graded plates. The high precision and versatility of the present method have manifested its great potential applications in strain-based or stress-based reliability analysis, optimization design, fatigue analysis, and fracture analysis of FGM plates, and other related fields.

Keywords: functionally graded material plate; spectral displacement formulation; isogeometric analysis; Chebyshev series

check for updates

Citation: Yang, S.; Sun, X.; Cai, Z.; Peng, H.; Zhang, Y. High-Precision Isogeometric Static Bending Analysis of Functionally Graded Plates Using a New Quasi-3D Spectral Displacement Formulation. *Appl. Sci.* **2023**, *13*, 6412. https://doi.org/10.3390/app13116412

Academic Editor: Motoharu Fujigaki

Received: 11 May 2023
Revised: 23 May 2023
Accepted: 23 May 2023
Published: 24 May 2023

1. Introduction

Functionally graded materials (FGMs) are heterogeneous materials characterized by gradually changing composition and material properties. FGMs can effectively avoid stress concentration between interfaces and are suitable for applications requiring conflicting properties. Due to their exceptional mechanical strength, high temperature resistance, and other characteristics, FGMs are widely used in various fields, such as aerospace equipment, electronic equipment, automobile engines, and medical equipment [1,2].

Mechanical analyses of functionally graded material (FGM) plates have been extensively discussed in the past decades using various theories [2–4]. The classical plate theory (CPT) [4], known as Kirchhoff theory, is only suitable for analyzing thin FGM plates where shear effects can be ignored. The first-order shear deformation theory (FSDT) [5], developed by Mindlin and Reissner, can handle the mechanical analyses of moderately thick FGM plates. However, problem-dependent shear correction factors are usually necessary to improve the accuracy. In addition, applying FSDT to thin plates leads to troublesome shear locking problems. Many higher-order shear deformation theories (HSDTs) have been proposed to analyze thick FGM plates, such as the third-order shear deformation theory (TSDT) [6,7], the fifth-order shear deformation theory, the nth-order shear deformation theory [8,9], the sinusoidal shear deformation theory, the exponential shear deformation theory, and the hyperbolic shear deformation theory [10–14]. Traction-free boundary conditions on the top and bottom surfaces are satisfied automatically in these HSDTs; thus, using shear correction factors becomes unnecessary. Generally, HSDTs also provide more accurate displacement and stress results than CPT and FSDT.

Carrera et al. [15] demonstrated the importance of the thickness stretching effect in analyzing FGM plates and shells and introduced the quasi-3D Carrera's unified formula (CUF). CUF expands all displacement components as Taylor series in the thickness direction; adjustable precision can be achieved by alternating the truncation numbers. Quasi-3D HSDTs have also been proposed. Zenkour [16] developed a quasi-3D trigonometric shear deformation theory and presented benchmark solutions for the bending of exponential FGM rectangular plates. Matsunaga [17,18] constructed a quasi-3D theory based on power series expansion for the vibration and buckling analyses of FGM plates and shallow shells, and the effects of shear deformation and rotatory inertia were investigated. Using a new quasi-3D theory, Talha and Singh [19] developed a nine-node isoparametric element for bending and free vibration analyses of FGM plates; the influences of aspect ratio, thickness ratio, volume fraction index, and boundary conditions were studied. Mantari and Soares [20] proposed a general formulation in which various quasi-3D theories can be formulated using combined polynomial, trigonometric, or hybrid functions [21,22]. Thai and Kim [23] constructed a quasi-3D sinusoidal shear deformation theory with five unknowns, in which the transverse displacement is divided into bending, shear, and stretching parts to reduce the number of unknowns and overcome the shear locking problem. Similarly, Thai [24], Hebali [25], Bessaim [26] and Bennoun [27] employed hyperbolic functions to construct shear-locking-free quasi-3D shear deformation theories. Belabed [28] and Mantari [29,30] presented a quasi-3D shear deformation theory by combining the polynomial and hyperbolic, or sinusoidal and hyperbolic functions. Neves and Ferreira et al. [31–33] combined polynomials and trigonometric functions to formulate various quasi-3D shear deformation theories. Farzam-Rad et al. [34] presented a new simple and efficient quasi-3D shear deformation theory with only five unknowns. As the thickness stretching effect is well accounted for, these quai-3D HSDTs generally show improved accuracy compared to conventional HSDTs.

This paper aims to develop a new high-precision quasi-3D shear deformation theory, called the spectral displacement formulation (SDF) [35], for the static bending analyses of FGM plates. The displacement fields in the thickness direction are expanded using the Chebyshev series. Similar to the CUF, the SDF is capable of hierarchical refinement to approach exact 3D solutions, and it can satisfy traction-free boundary conditions without additional modifications. Compared with commonly used shear deformation theories, such as CPT, FSDT, HSDTs, and most of the quasi-3D HSDTs, the SDF supplies higher accuracy, especially for the strain and stress analyses. The SDF is extended from the CPT and naturally free from shear locking. This feature guarantees that the SDF has versatility for thin and thick FGM plates and offers a flexible balance between accuracy and computational cost that can be adjusted by changing the truncation numbers. A non-uniform rational B-splines (NURBS)-based isogeometric analysis (IGA) method [36] is implemented to satisfy the in-plane C^1-continuity requirement of the SDF and further enhance the present method's applicability to complex plate geometries. In view of the remarkable precision and versatility, the SDF-based IGA method has significant potential in various applications, e.g., strain-based or stress-based reliability analysis, optimization design, fatigue analysis, and fracture analysis [37,38].

This paper is organized as follows: Section 2 details the basic assumptions of the SDF and presents the integral governing equations based on d'Alembert's principle and the principle of virtual work. Section 3 briefly introduces the concept of NURBS and derives the discrete governing equations. Section 4 presents numerical examples and discussions. The conclusions are summarized in Section 5.

2. Fundamental Assumptions and Formulations

2.1. Functionally Graded Material Plate

Consider an FGM plate shown in Figure 1 with a constant thickness of h and midplane located in the oxy plane. The FGM plate consists of ceramic and metal materials in the direction of thickness according to the following power law [39]:

$$\begin{matrix} \upsilon_{\mathrm{c}} = (1/2 + z/h)^{g} \\ \upsilon_{\mathrm{m}} = 1 - \upsilon_{\mathrm{c}} \end{matrix} \quad , \quad z \in [-h/2, h/2] \tag{1}$$

where υ_{c} and υ_{m} are the volume fractions of the ceramic and the metal, respectively. g is the gradient index that controls the variation of material properties in the thickness direction.

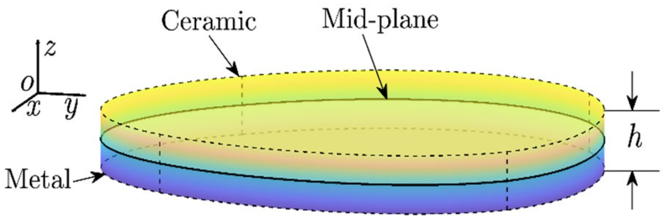

Figure 1. Functionally graded material plate.

The rule of mixtures [2] is applied to determine the equivalent material properties of the FGM plate according to the following relationship:

$$(E, \nu, \rho) = (E_{\mathrm{c}}, \nu_{\mathrm{c}}, \rho_{\mathrm{c}})\upsilon_{\mathrm{c}} + (E_{\mathrm{m}}, \nu_{\mathrm{m}}, \rho_{\mathrm{m}})\upsilon_{\mathrm{m}} \tag{2}$$

where E_{c}, ν_{c}, ρ_{c} represent the elastic modulus, Poisson's ratio, and mass density of the ceramic, respectively, and E_{m}, ν_{m}, ρ_{m} correspond to the elastic modulus, Poisson's ratio, and mass density of the metal, respectively. The resulting values E, ν and ρ represent the equivalent properties of the FGM plate.

2.2. Spectral Displacement Formulation

For high-precision analyses of thick FGM plates, as well as for the stress analyses of thin FGM plates, refined shear deformation theories are necessary [4]. In this paper, the displacement fields are expanded into the following spectral series:

$$\left\{ \begin{array}{l} u = u_0 + \sum_{i=1}^{M} (u_i - w_{i-1,x})\kappa_i(z) + \sum_{i=M+1}^{N} u_i\kappa_i(z) \\ v = v_0 + \sum_{i=1}^{M} (v_i - w_{i-1,y})\kappa_i(z) + \sum_{i=M+1}^{N} v_i\kappa_i(z) \\ w = \sum_{i=1}^{M} w_{i-1}\kappa_i'(z) \end{array} \right. \tag{3}$$

where u, v, and w are displacements in the x, y, and z directions; $\{u_i\}_{i=0}^{N}$, $\{v_i\}_{i=0}^{N}$, and $\{w_i\}_{i=0}^{M-1}$ are basic unknows. $\{\kappa_i(z)\}_{i=1}^{N}$ are the spectral bases with the first constant term omitted. $(\ )'$ represents the first-order derivative, while $(\ )_{,x}$ and $(\ )_{,y}$ indicate first-order partial derivatives with respect to x and y, respectively. M and N are the truncation numbers for the transverse and the in-plane displacement fields, $M \leq N$. Equation (3) can be rearranged in the following vector form:

$$\begin{array}{l} \mathbf{u} = \mathbf{u}_0 + \sum_{i=1}^{M} \mathbf{A}_i(z)\mathbf{u}_i + \sum_{i=M+1}^{N} \mathbf{A}_i(z)\mathbf{u}_i \\ \mathbf{A}_i(z) = \mathrm{diag}\left[\kappa_i(z), \kappa_i(z), \kappa_i'(z)\right] \end{array} \tag{4}$$

where $\mathbf{u} = [u, v, w]^{\mathrm{T}}$, $\{\mathbf{u}_i\}_{i=0}^{N}$ are the generalized displacements defined as follows:

$$\mathbf{u}_i = \left\{ \begin{array}{ll} \left[u_i - w_{i-1,x}, v_i - w_{i-1,y}, w_{i-1}\right]^{\mathrm{T}}, & 1 \leq i \leq M \\ \left[u_i, v_i, 0\right]^{\mathrm{T}}, & i = 0 \text{ and } M+1 \leq i \leq N \end{array} \right. \tag{5}$$

The infinitesimal strain fields can be expressed as [40]

$$\begin{array}{l} \boldsymbol{\varepsilon} = \boldsymbol{\varepsilon}_0 + \sum_{i=1}^{M} \mathbf{B}_i(z)\boldsymbol{\varepsilon}_i + \sum_{i=M+1}^{N} \mathbf{B}_i(z)\boldsymbol{\varepsilon}_i \\ \mathbf{B}_i(z) = \mathrm{diag}\left[\kappa_i(z), \kappa_i(z), \kappa_i''(z), \kappa_i'(z), \kappa_i'(z), \kappa_i(z)\right] \end{array} \tag{6}$$

where $\boldsymbol{\varepsilon} = \left[\varepsilon_{xx}, \varepsilon_{yy}, \varepsilon_{zz}, \gamma_{yz}, \gamma_{xz}, \gamma_{xy}\right]^{\mathrm{T}}$, $\{\boldsymbol{\varepsilon}_i\}_{i=0}^{N}$ are generalized strains in the following form:

$$\boldsymbol{\varepsilon}_i = \begin{cases} \begin{array}{l} \left[u_{i,x} - w_{i-1,xx},\ v_{i,y} - w_{i-1,yy}, w_{i-1}, \right. \\ \quad \left. v_i, u_i, u_{i,y} + v_{i,x} - 2w_{i-1,xy}\right]^{\mathrm{T}} \end{array}, & 1 \le i \le M \\ \left[u_{i,x}, v_{i,y}, 0, v_i, u_i, u_{i,y} + v_{i,x}\right]^{\mathrm{T}}, & i = 0 \text{ and } M+1 \le i \le N \end{cases} \tag{7}$$

Applying the 3D elastic constitutive relations [40], the stress fields are expressed as

$$\begin{array}{l} \boldsymbol{\sigma} = \mathbf{D}\boldsymbol{\varepsilon} = \mathbf{D}\boldsymbol{\varepsilon}_0 + \sum_{i=1}^{M} \mathbf{D}\mathbf{B}_i(z)\boldsymbol{\varepsilon}_i + \sum_{i=M+1}^{N} \mathbf{D}\mathbf{B}_i(z)\boldsymbol{\varepsilon}_i \\ \mathbf{D} = \begin{bmatrix} \mathbf{D}_{\mathrm{n}} & 0_{3\times3} \\ 0_{3\times3} & \mathbf{D}_{\mathrm{s}} \end{bmatrix}, \quad (\mathbf{D}_{\mathrm{n}})_{ij} = \lambda + 2\mu\delta_{ij}, \quad (\mathbf{D}_{\mathrm{s}})_{ij} = \mu\delta_{ij} \end{array} \tag{8}$$

where $\boldsymbol{\sigma} = \left[\sigma_{xx}, \sigma_{yy}, \sigma_{zz}, \sigma_{yz}, \sigma_{xz}, \sigma_{xy}\right]^{\mathrm{T}}$, δ_{ij} is the Kronecker symbol. $\lambda = E\nu/(1+\nu)/(1-2\nu)$ and $\mu = E/(1+\nu)/2$ are Lamé parameters.

In this paper, the Chebyshev polynomials of the first kind are taken as the spectral bases whose first-order derivatives are Chebyshev polynomials of the second kind. Specifically, Chebyshev polynomials [41] of the first kind on $[-h/2, h/2]$ are defined as [41]

$$\begin{array}{l} T_0(z) = 1, \quad T_1(z) = \frac{2z}{h} \\ T_i(z) = \frac{4z}{h} T_{i-1}(z) - T_{i-2}(z), \quad i \ge 2 \end{array} \tag{9}$$

and Chebyshev polynomials of the second kind are defined as [41]

$$\begin{array}{l} U_0(z) = 1, \quad U_1(z) = \frac{4z}{h} \\ U_i(z) = \frac{4z}{h} U_{i-1}(z) - U_{i-2}(z), \quad i \ge 2 \end{array} \tag{10}$$

Figure 2 shows the function shapes of the first five Chebyshev bases. It is also noted that the SDF is inherently an extension of the CPT and thus naturally free from shear-locking, similarly as already been extensively stated by Thai [42] and Nguyen [43], among others.

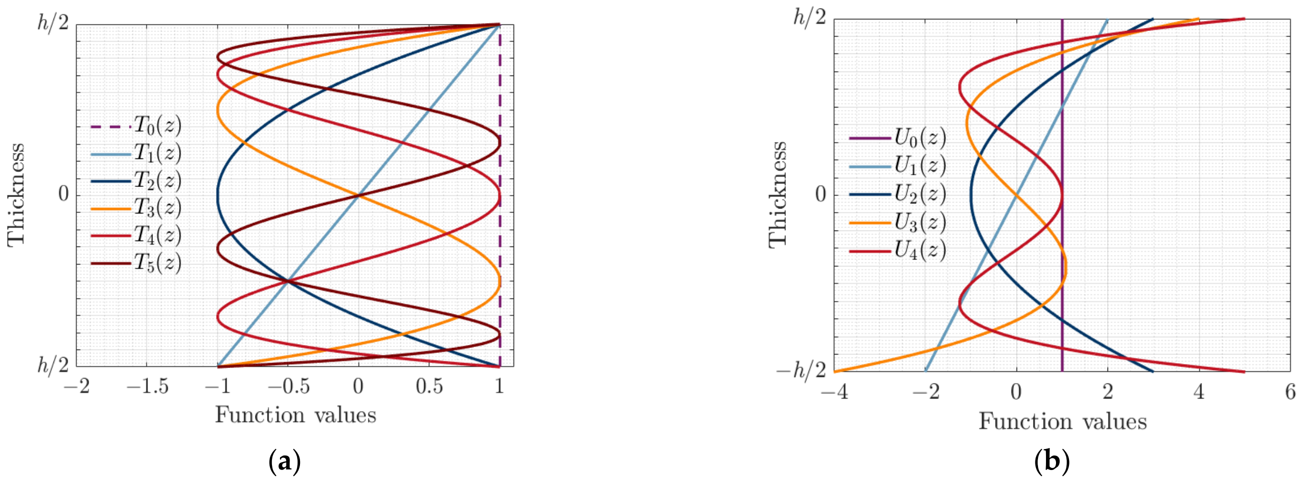

Figure 2. Chebyshev polynomials. (**a**) Chebyshev polynomials of the first kind; (**b**) Chebyshev polynomials of the second kind.

2.3. Integral Governing Equations

Assuming the top surface of the FGM plate is subjected to a distributed transverse force $\varrho(x, y)$, the integral governing equations of the FGM plate can be derived based on the d'Alembert principle and the principle of virtual work [40]. These equations can be written as

$$\int_V \delta\boldsymbol{\varepsilon}^{\mathrm{T}}\boldsymbol{\sigma}\mathrm{d}v = \int_\Omega \left[\sum_{i=1}^{M} \delta w_{i-1}\kappa_i'\left(\frac{h}{2}\right)\right]\varrho(x,y)\mathrm{d}a \tag{11}$$

where V and Ω represent the volume and the midplane of the FGM plate, respectively. Combined with Equations (4)–(8), Equation (11) can be rearranged as

$$\int_\Omega \delta\tilde{\boldsymbol{\varepsilon}}^{\mathrm{T}}\tilde{\mathbf{D}}\tilde{\boldsymbol{\varepsilon}}\mathrm{d}a = \int_\Omega \delta\tilde{\mathbf{u}}^{\mathrm{T}}\boldsymbol{\vartheta}\varrho\mathrm{d}a \tag{12}$$

where $\tilde{\mathbf{D}}$ is the modulus matrix, $\boldsymbol{\vartheta}$ is a load indicator vector, and

$$\begin{gathered}
\tilde{\mathbf{u}} = \begin{Bmatrix} \mathbf{u}_0 \\ \vdots \\ \mathbf{u}_N \end{Bmatrix}, \quad \tilde{\boldsymbol{\varepsilon}} = \begin{Bmatrix} \boldsymbol{\varepsilon}_0 \\ \vdots \\ \boldsymbol{\varepsilon}_N \end{Bmatrix}, \quad \tilde{\mathbf{D}} = \begin{bmatrix} \tilde{\mathbf{D}}_{00} & \cdots & \tilde{\mathbf{D}}_{0N} \\ \vdots & \ddots & \vdots \\ \tilde{\mathbf{D}}_{N0} & \cdots & \tilde{\mathbf{D}}_{NN} \end{bmatrix}, \quad \tilde{\mathbf{D}}_{ji} = \left(\tilde{\mathbf{D}}_{ij}\right)^{\mathrm{T}}, \ \forall i,j \in [0,N] \\
\left(\tilde{\mathbf{D}}_{00}, \tilde{\mathbf{D}}_{0j}, \tilde{\mathbf{D}}_{ij}\right) = \int_{-\frac{h}{2}}^{\frac{h}{2}} \left(\mathbf{D}, \mathbf{D}\mathbf{B}_j(z), \mathbf{B}_i(z)\mathbf{D}\mathbf{B}_j(z)\right)\mathrm{d}z, \quad 1 \le i,j \le N \\
(\boldsymbol{\vartheta})_s = \begin{cases} \kappa_i'(h/2), & s = 3(i+1),\ i \in [1,M] \\ 0, & \text{otherwise} \end{cases}
\end{gathered} \tag{13}$$

3. NURBS-Based Isogeometric Analysis

IGA was proposed by Hughes et al. [44] to seamlessly link computer-aided engineering (CAE) and computer-aided design (CAD). In IGA, the widely used NURBS basis functions in CAD are directly applied to numerical simulations; therefore, potential geometric errors can be eliminated. In addition, NURBS-based IGA conveniently fulfills continuity requirements of arbitrary orders that can be challenging to achieve in the conventional finite element method. The SDF proposed in this paper requires at least C^1-continuity, which is readily satisfied using NURBS-based IGA.

3.1. A Brief on NURBS

A knot vector $\boldsymbol{\Sigma} = \{\zeta_1, \ldots, \zeta_{n+p+1}\}$ is assigned on the one-dimensional parameter axis ζ, where ζ_i is the ith knot, and $\zeta_{i+1} \ge \zeta_i$. Knots in $\boldsymbol{\Sigma}$ may be repeated. An open knot vector is usually used, where the start and end knots repeat p + 1 times to create additional control points at the ends. The knot vector $\boldsymbol{\Sigma}$ recursively defines a group of one-dimensional polynomial B-splines as follows [44,45]:

$$\begin{gathered}
\mathcal{N}_{i,0}(\zeta) = \begin{cases} 1, & \zeta \in [\zeta_i, \zeta_{i+1}) \\ 0, & \text{otherwise} \end{cases} \\
\mathcal{N}_{i,p}(\zeta) = \frac{\zeta - \zeta_i}{\zeta_{i+p} - \zeta_i}\mathcal{N}_{i,p-1}(\zeta) + \frac{\zeta_{i+p+1} - \zeta}{\zeta_{i+p+1} - \zeta_{i+1}}\mathcal{N}_{i+1,p-1}(\zeta), \quad p \ge 1
\end{gathered} \tag{14}$$

where p and n are the order and the total number of the B-splines, respectively. $i = 1, \ldots, n$ denotes the sequence number. Polynomial B-splines cannot accurately represent conic curves; hence, rational B-splines are constructed as [44,45]

$$\mathcal{R}_{i,p}(\zeta) = \frac{\varpi_i \mathcal{N}_{i,p}(\zeta)}{\sum_{j=1}^{n} \varpi_j \mathcal{N}_{j,p}(\zeta)} \tag{15}$$

where the constants $\varpi_i > 0$ denote the weights. The weights $\{\varpi_i\}_{i=1}^n$, the knot vector $\boldsymbol{\Sigma}$, and the order p. define a group of rational B-splines. The rational B-splines based on non-uniform knot vectors are called NURBS.

Multi-dimensional NURBS basis functions used to discretize multivariable functions can be readily obtained by tensor product operations. Specifically, the NURBS representation of a bivariable function can be simplified as [44,45]

$$\begin{aligned} \mathbf{s}(\zeta,\eta) &= \sum_{\lceil \mathbf{i} \rceil=1}^{Q} \mathbf{s}_{\lceil \mathbf{i} \rceil} \mathcal{R}_{\lceil \mathbf{i} \rceil}(\zeta,\eta) \\ \mathcal{R}_{\lceil \mathbf{i} \rceil}(\zeta,\eta) &= \mathcal{R}_{i_1,p_1}(\zeta)\mathcal{R}_{i_2,p_2}(\eta) \end{aligned} \tag{16}$$

where $\lceil \mathbf{i} \rceil$ is the lexicographical order associated with the two-tuple $\mathbf{i} = (i_1, i_2)$, which contains the sequence numbers of ζ-dimensional and η–dimensional NURBS basis functions. The $\mathbf{s}_{\lceil \mathbf{i} \rceil}$ represents control points or control vectors, while $\mathcal{R}_{\lceil \mathbf{i} \rceil}$ represents the two-dimensional (2D) NURBS basis functions. $Q = n_1 \times n_2$ denotes the total number of 2D NURBS basis functions. Additionally, p_1 and p_2, along with n_1 and n_2, indicate the orders and the total numbers of the one-dimensional (1D) NURBS basis functions in the ζ and η directions, respectively.

NURBS basis functions are widely used for creating parametric representations of geometric models [44,45]. Figure 3a,b illustrate an instance of a 2D NURBS plane in Euclidean and parameter space, respectively. For a deeper understanding of NURBS and NURBS-based IGA, refer to the works of Piegl and Tiller [45], Farin [46], and Hughes and Cottrell [44].

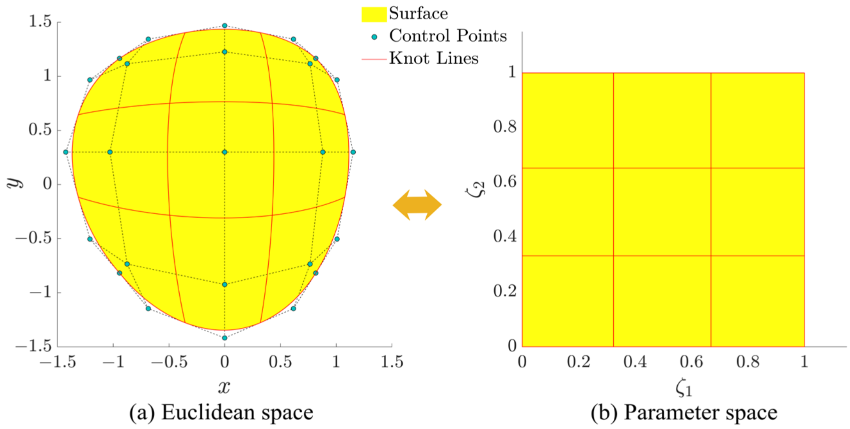

Figure 3. Two-dimensional NURBS plane.

3.2. Discrete Governing Equations

The analysis of the FGM plate is simplified to a 2D problem using the process outlined in Section 2. The midplane geometry of the FGM plate is modeled based on 2D NURBS basis functions, which can be expressed as

$$\Omega = \left\{ \mathbf{x} = (x,y) \middle| \mathbf{x}(\boldsymbol{\zeta}) = \sum_{\lceil \mathbf{i} \rceil=1}^{Q} \mathbf{x}_{\lceil \mathbf{i} \rceil} \mathcal{R}_{\lceil \mathbf{i} \rceil}(\boldsymbol{\zeta}), \quad \boldsymbol{\zeta} = (\zeta,\eta) \in \hat{\Omega} \right\} \tag{17}$$

where $\mathbf{x}_{\lceil \mathbf{i} \rceil}$ are the geometric control points, and $\hat{\Omega}$ is the mapping of the midplane Ω in the parameter space. The displacement fields are discretized using 2D NURBS basis functions calculated as

$$\mathbf{q}(\boldsymbol{\zeta}) = \sum_{\lceil \mathbf{i} \rceil=1}^{Q} \mathbf{q}_{\lceil \mathbf{i} \rceil} \mathcal{R}_{\lceil \mathbf{i} \rceil}(\boldsymbol{\zeta}) \tag{18}$$

where $\mathbf{q} = [u_0, \ldots, u_N, v_0, \ldots, v_N, w_0, \ldots, w_{M-1}]^{\mathrm{T}}$ is a vector that collects all the basic unknowns. $\mathbf{q}_{\lceil \mathbf{i} \rceil}$ are the control vectors. Combined with Equations (4) and (6), the displacement and the strain fields can be expressed as

$$\begin{aligned} \tilde{\mathbf{u}}(\boldsymbol{\zeta}) &= \sum_{\lceil \mathbf{i} \rceil=1}^{Q} \mathbf{U}_{\lceil \mathbf{i} \rceil}(\boldsymbol{\zeta}) \mathbf{q}_{\lceil \mathbf{i} \rceil} \\ \tilde{\boldsymbol{\varepsilon}}(\boldsymbol{\zeta}) &= \sum_{\lceil \mathbf{i} \rceil=1}^{Q} \mathbf{E}_{\lceil \mathbf{i} \rceil}(\boldsymbol{\zeta}) \mathbf{q}_{\lceil \mathbf{i} \rceil} \end{aligned} \tag{19}$$

where $\mathbf{U}_{\lceil\mathbf{i}\rceil}$ and $\mathbf{E}_{\lceil\mathbf{i}\rceil}$ are sparse block coefficient matrices, the nonzero elements of which are listed as

$$\begin{aligned}
&\left(\mathbf{U}_{\lceil\mathbf{i}\rceil}\right)_{11} = \left(\mathbf{U}_{\lceil\mathbf{i}\rceil}\right)_{2,N+2} = \mathcal{R}_{\lceil\mathbf{i}\rceil};\\
&\left(\mathbf{U}_{\lceil\mathbf{i}\rceil}\right)_{3i+1,i+1} = \left(\mathbf{U}_{\lceil\mathbf{i}\rceil}\right)_{3i+2,N+i+2} = \left(\mathbf{U}_{\lceil\mathbf{i}\rceil}\right)_{3i+3,2N+i+2} = \mathcal{R}_{\lceil\mathbf{i}\rceil},\\
&\left(\mathbf{U}_{\lceil\mathbf{i}\rceil}\right)_{3i+1,2N+i+2} = -\mathcal{R}_{\lceil\mathbf{i}\rceil,x}, \quad \left(\mathbf{U}_{\lceil\mathbf{i}\rceil}\right)_{3i+2,2N+i+2} = -\mathcal{R}_{\lceil\mathbf{i}\rceil,y}, \quad 1 \le i \le M;\\
&\left(\mathbf{U}_{\lceil\mathbf{i}\rceil}\right)_{3i+1,i+1} = \left(\mathbf{U}_{\lceil\mathbf{i}\rceil}\right)_{3i+2,N+i+2} = \mathcal{R}_{\lceil\mathbf{i}\rceil}, \quad M+1 \le i \le N.
\end{aligned} \tag{20}$$

and

$$\begin{aligned}
&\left(\mathbf{E}_{\lceil\mathbf{i}\rceil}\right)_{11} = \left(\mathbf{E}_{\lceil\mathbf{i}\rceil}\right)_{6,N+2} = \mathcal{R}_{\lceil\mathbf{i}\rceil,x}, \left(\mathbf{E}_{\lceil\mathbf{i}\rceil}\right)_{2,N+2} = \left(\mathbf{E}_{\lceil\mathbf{i}\rceil}\right)_{61} = \mathcal{R}_{\lceil\mathbf{i}\rceil,y};\\
&\left(\mathbf{E}_{\lceil\mathbf{i}\rceil}\right)_{6i+1,i+1} = \left(\mathbf{E}_{\lceil\mathbf{i}\rceil}\right)_{6i+6,N+i+2} = \mathcal{R}_{\lceil\mathbf{i}\rceil,x}, \quad \left(\mathbf{E}_{\lceil\mathbf{i}\rceil}\right)_{6i+1,2N+i+2} = -\mathcal{R}_{\lceil\mathbf{i}\rceil,xx},\\
&\left(\mathbf{E}_{\lceil\mathbf{i}\rceil}\right)_{6i+2,N+i+2} = \left(\mathbf{E}_{\lceil\mathbf{i}\rceil}\right)_{6i+6,i+1} = \mathcal{R}_{\lceil\mathbf{i}\rceil,y}, \quad \left(\mathbf{E}_{\lceil\mathbf{i}\rceil}\right)_{6i+2,2N+i+2} = -\mathcal{R}_{\lceil\mathbf{i}\rceil,yy},\\
&\left(\mathbf{E}_{\lceil\mathbf{i}\rceil}\right)_{6i+3,2N+i+2} = \left(\mathbf{E}_{\lceil\mathbf{i}\rceil}\right)_{6i+4,N+i+2} = \left(\mathbf{E}_{\lceil\mathbf{i}\rceil}\right)_{6i+5,i+1} = \mathcal{R}_{\lceil\mathbf{i}\rceil},\\
&\left(\mathbf{E}_{\lceil\mathbf{i}\rceil}\right)_{6i+6,2N+i+2} = -2\mathcal{R}_{\lceil\mathbf{i}\rceil,xy}, \quad 1 \le i \le M;\\
&\left(\mathbf{E}_{\lceil\mathbf{i}\rceil}\right)_{6i+1,i+1} = \left(\mathbf{E}_{\lceil\mathbf{i}\rceil}\right)_{6i+6,N+i+2} = \mathcal{R}_{\lceil\mathbf{i}\rceil,x},\\
&\left(\mathbf{E}_{\lceil\mathbf{i}\rceil}\right)_{6i+2,N+i+2} = \left(\mathbf{E}_{\lceil\mathbf{i}\rceil}\right)_{6i+6,i+1} = \mathcal{R}_{\lceil\mathbf{i}\rceil,y},\\
&\left(\mathbf{E}_{\lceil\mathbf{i}\rceil}\right)_{6i+4,N+i+2} = \left(\mathbf{E}_{\lceil\mathbf{i}\rceil}\right)_{6i+5,i+1} = \mathcal{R}_{\lceil\mathbf{i}\rceil}, \quad M+1 \le i \le N.
\end{aligned} \tag{21}$$

Substituting Equation (19) into Equation (12), the discrete governing equations of the FGM plate can be obtained as

$$\begin{aligned}
&\textstyle\sum_{\lceil\mathbf{j}\rceil=1}^{Q} \mathbf{K}_{\lceil\mathbf{i}\rceil\lceil\mathbf{j}\rceil}\mathbf{q}_{\lceil\mathbf{j}\rceil} = \varrho_{\lceil\mathbf{i}\rceil}, \quad \forall\lceil\mathbf{i}\rceil \in [1, Q]\\
&\mathbf{K}_{\lceil\mathbf{i}\rceil\lceil\mathbf{j}\rceil} = \textstyle\int_{\hat{\Omega}} \mathbf{E}_{\lceil\mathbf{i}\rceil}^{\mathrm{T}}\tilde{\mathbf{D}}\mathbf{E}_{\lceil\mathbf{j}\rceil} J_{\mathrm{a}} \mathrm{d}\hat{a}, \quad \varrho_{\lceil\mathbf{i}\rceil} = \textstyle\int_{\hat{\Omega}} \mathbf{U}_{\lceil\mathbf{i}\rceil}^{\mathrm{T}} \boldsymbol{\vartheta}\varrho J_{\mathrm{a}} \mathrm{d}\hat{a}
\end{aligned} \tag{22}$$

where J_{a} represents the Jacobian determinant [47], $\mathbf{K}_{\lceil\mathbf{i}\rceil\lceil\mathbf{j}\rceil}$ and $\varrho_{\lceil\mathbf{i}\rceil}$ are block stiffness matrices and load vectors, respectively. Equation (22) can be further arranged using the established lexicographical order into a global form as

$$\mathbf{Kd} = \mathbf{f} \tag{23}$$

where $\mathbf{K}$, $\mathbf{d}$, and $\mathbf{f}$ are the global stiffness matrix, displacement and load vector, respectively, assembled from $\mathbf{K}_{\lceil\mathbf{i}\rceil\lceil\mathbf{j}\rceil}$, $\mathbf{q}_{\lceil\mathbf{j}\rceil}$, and $\boldsymbol{\rho}_{\lceil\mathbf{i}\rceil}$. The local support property of the NURBS basis functions ensures the sparseness of the stiffness matrix $\mathbf{K}$ [44,45].

4. Numerical Examples

In this section, examples of square, rectangular, circular, and L-shaped FGM plates are used to demonstrate the effectiveness of the proposed methodology. Specifically, in Section 4.1, the square plate example is utilized to verify the convergence performance of the SDF in terms of the two truncation numbers. In Section 4.2, the converged results of the rectangular plates are compared with exact 3D elastic solutions to validate the high accuracy of the SDF. In Sections 4.3 and 4.4, the circular and the L-shaped plate examples are tested to illustrate the application of the SDF-based IGA to analyze FGM plates with multi-patch and complex geometries. Table 1 shows the properties of the relevant materials.

Table 1. Material properties of ceramics and metals.

	Young's Modulus (GPa)	Poisson's Ratio	Density (kg/m^3)
Al	70	0.3	2707
Ti	110.25	0.288	-
Al_2O_3	380	0.3	3800
ZrO_2	278.41	0.288	-
SiC	427	0.17	3210

The penalty method is used to impose boundary conditions and handle patch coupling, in which the penalty coefficient is 10^4 times the maximum element of related stiffness matrices [44]. The k-refinement strategy [44] is applied to meshing the models and $(p+1) \times (q+1)$ in-plane Gaussian integration points are used in each element [48]. The number of integration points in the thickness direction is determined according to the value of the gradient index. The codes were compiled using MATLAB 9.10 and run on a computer with Intel(R) Core (TM) i7-9750H CPU (2.60 GHz), Win10 64-bit OS, 32 GB RAM, and 12 threads.

As a preliminary to further discussions, the shear-locking-free property of the proposed SDF is demonstrated by considering a homogeneous square plate with length a, thickness h, and elastic properties $E = 1.092$ GPa, $v = 0$. The plate is subjected to a uniformly distributed load with amplitude $\varrho_0 = 1$ N. Both simply supported and clamped boundary conditions are considered; SDF-based IGA using second-order NURBS basis functions with a 10×10 mesh and SDF truncation numbers $M = 3$ and $N = 3$ prove accurate enough.

Figure 4 compares the results obtained using the SDF-based IGA in this paper with the reference solutions presented in the relevant literature [49]. It is seen that for small aspect ratios, the central deflection results obtained using the SDF-based IGA are close to those of the FSDT-based IGA, which are considered to be accurate in practice. As the aspect ratio increases, the FSDT-based IGA displays obvious locking behavior. At the same time, the results obtained using the SDF-based IGA conform well with the CPT-based solutions for thin plates, demonstrating the shear-locking-free property.

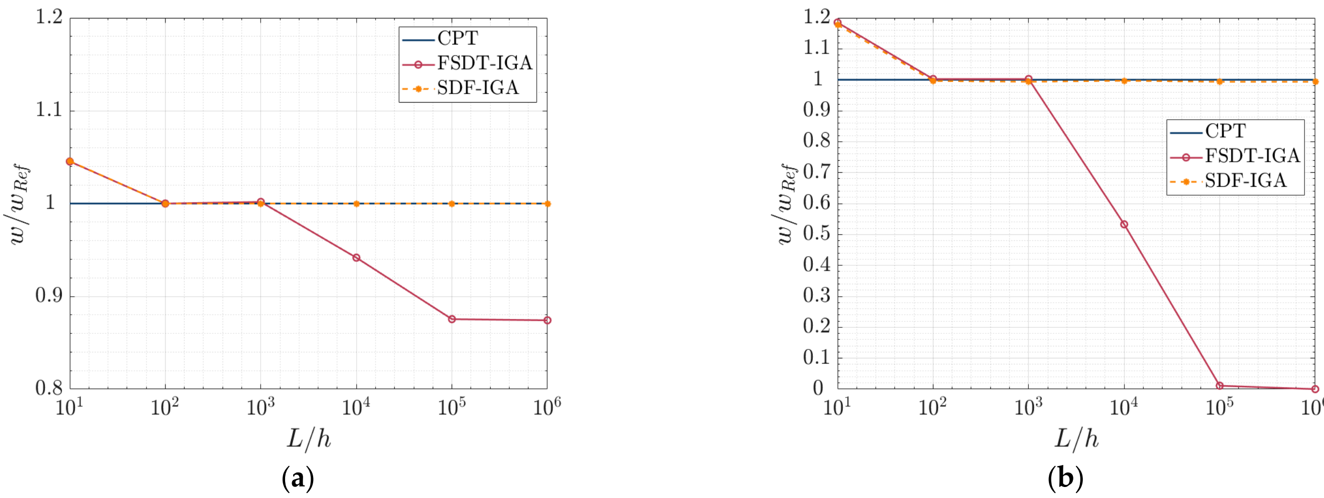

Figure 4. Central deflections of a homogeneous square plate with various aspect ratios. (**a**) Simply supported; (**b**) clamped.

4.1. Square Al_2O_3 Plate

Consider a fully simply supported square plate with length a, thickness h, as shown in Figure 5. The plate is assumed to be made of aluminum (Al) and aluminum oxide (Al_2O_3), and the corresponding material properties are listed in Table 1.

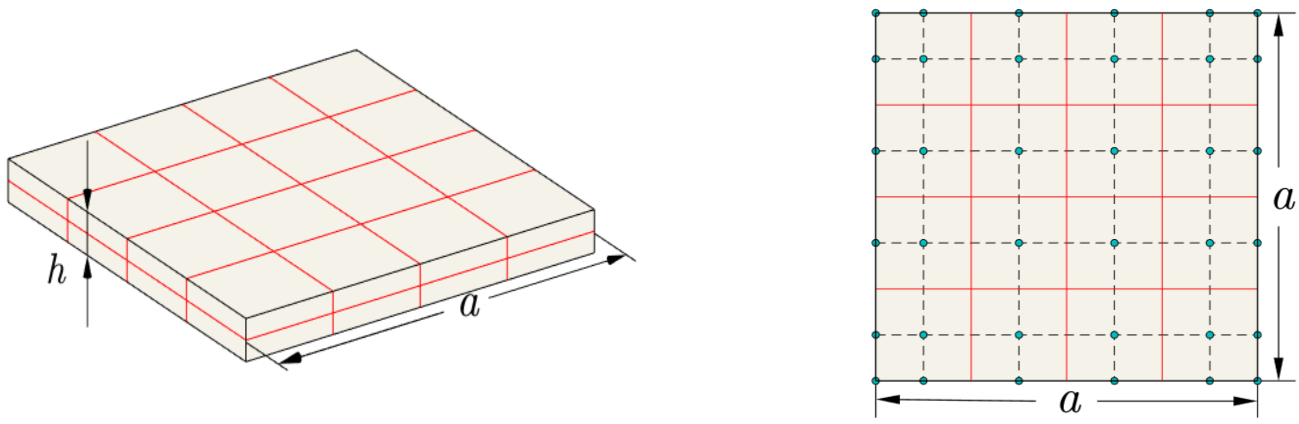

(**a**) (**b**)

Figure 5. Three-dimensional geometry and 2D NURBS midplane of a square plate. (**a**) Three-dimensional geometry; (**b**) 2D NURBS midplane.

Assuming the length $a = 1$, the thickness $h = 0.25$, and the gradient index $g = 10$, and the top surface of the plate is subjected to a transverse bi-sinusoidal load $\varrho_0 \sin(\pi x/a) \sin(\pi y/a)$ with $\varrho_0 = 4 \times 10^9$, numerical tests indicate that using fourth-order NURBS basis functions with a 10×10 mesh in the SDF-based IGA provide converged response results for any SDF truncation numbers.

Defining nondimensional deflection and stress responses as $\overline{w} = \frac{10h^3 E_c}{a^4 \varrho_0} w\left(\frac{a}{2}, \frac{a}{2}, 0\right)$, $\overline{\sigma}_{xx} = \frac{h}{a\varrho_0}\sigma_{xx}\left(\frac{a}{2}, \frac{a}{2}, \frac{h}{3}\right)$, $\overline{\tau}_{xz} = \frac{h}{a\varrho_0}\tau_{xz}\left(0, \frac{a}{2}, \frac{h}{6}\right)$, Figure 6 shows the convergence of the results with respect to the SDF truncation numbers. The deflection $\overline{w}$ converges as $M \geq 3$ and $N \geq 3$; however, for the normal stress $\overline{\sigma}_{xx}$ and the shear stress $\overline{\tau}_{xz}$, converged results can only be obtained by setting $M \geq 5$ and $N \geq 6$.

The converged nondimensional 3D responses are shown in Figure 7. It is noted that the shear stress $\overline{\tau}_{xz}$ on the top and bottom surfaces of the plate is zero, satisfying the traction-free boundary conditions [50].

As shown in Table 2, the nondimensional deflection and stress results for various gradient indexes and aspect ratios obtained using the SDF-based IGA ($M = 5$, $N = 6$) are compared with available references in the literature. Quasi-3D [15] represents results based on CUF; TSDT-IGA [42] represents IGA solutions based on Reddy's TSDT; FSDT [15] are analytical solutions based on the FSDT. It is found that all four methods yield generally acceptable deflection results. However, the FSDT is unable to provide accurate stress results for both thick and thin FGM plates. The TSDT-IGA method shows improved but limited accuracy stress results, especially for thick FGM plates. In all cases, the SDF-based IGA results conform very well with the quasi-3D results, indicating the accuracy and reliability of the present method.

4.2. Rectangular E-FGM Plate

Consider bending of simply supported exponentially functionally graded material (E-FGM) rectangular plates with Poisson's ratio $\nu = 0.3$ under a bi-sinusoidal transverse load. The nondimensional responses are defined as $[\overline{u}, \overline{v}, \overline{w}] = \frac{10E_0h^3}{a^4\varrho_0}[u, v, w](z)$, $[\overline{\sigma}_{xx}, \overline{\sigma}_{yy}] = \frac{h^2}{a^2\varrho_0}[\sigma_{xx}, \sigma_{yy}](z)$, $\overline{\tau}_{xy} = \frac{10h^2}{a^3\varrho_0}\tau_{xy}(z)$, $[\overline{\tau}_{yz}, \overline{\tau}_{xz}] = \frac{h}{a\varrho_0}[\tau_{yz}, \tau_{xz}](z)$, where a is the width, h is the thickness, ϱ_0 is the amplitude of the load. E_0 is the elasticity modulus on the bottom surface of the plate; however, the nondimensional responses are irrelevant to E_0 in practice; see Zenkour [15] for more details.

Using fourth-order NURBS basis functions and setting the SDF truncation numbers $M = 5$, $N = 6$ as described in Section 4.1. Assuming the gradient index $k = 0.5$, the width-to-thickness ratio $a/h = 4$, and the length-to-width ratio b/a ranging from 1 to 4, Figure 8 compares the displacement and stress results obtained using the SDF-based IGA with the exact 3D elasticity solutions provided by Zenkour [16]. It can be seen that the predicted results agree perfectly with the exact solutions, demonstrating the ability of the proposed method to supply sufficiently accurate and reliable results.

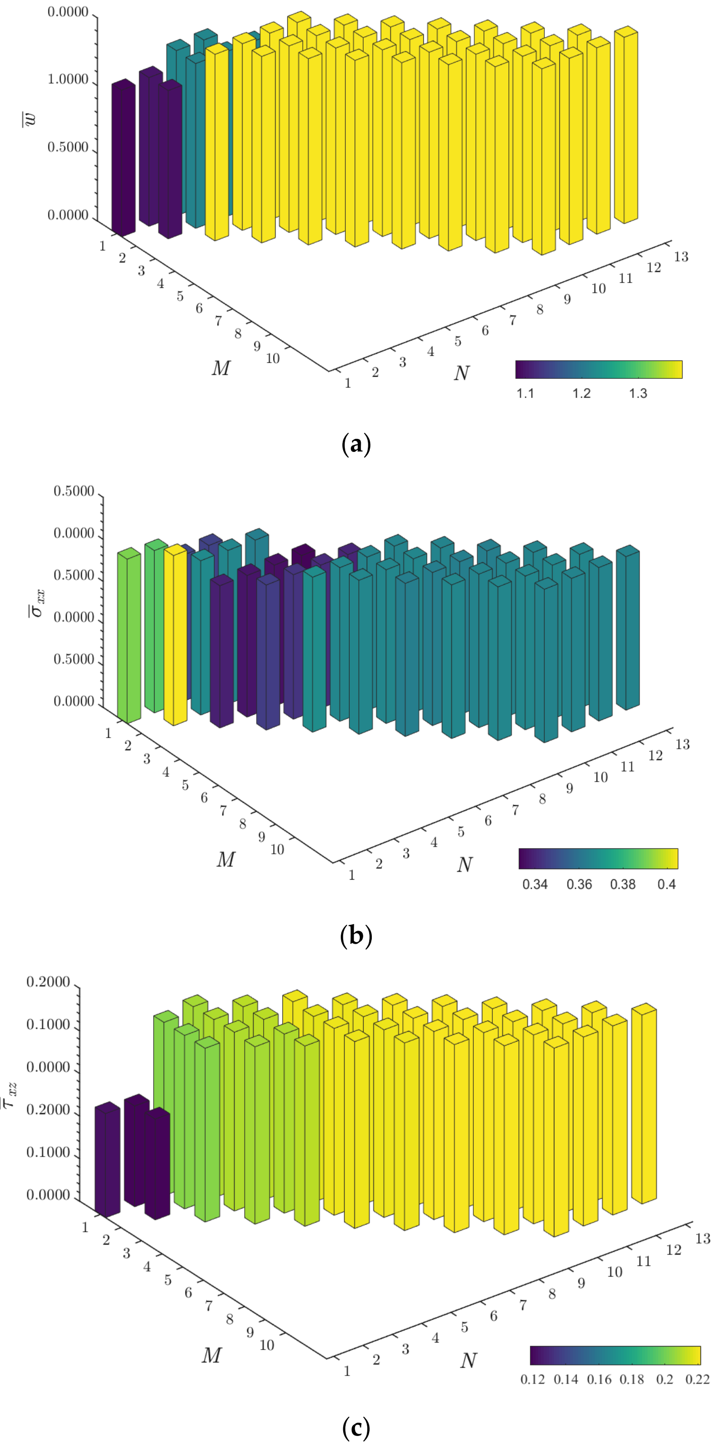

Figure 6. Convergence of nondimensional responses with respect to the SDF truncation numbers for Al/Al_2O_3 square plate. (**a**) Convergence of $\overline{w}$; (**b**) convergence of $\overline{\sigma}_{xx}$; (**c**) convergence of $\overline{\tau}_{xz}$.

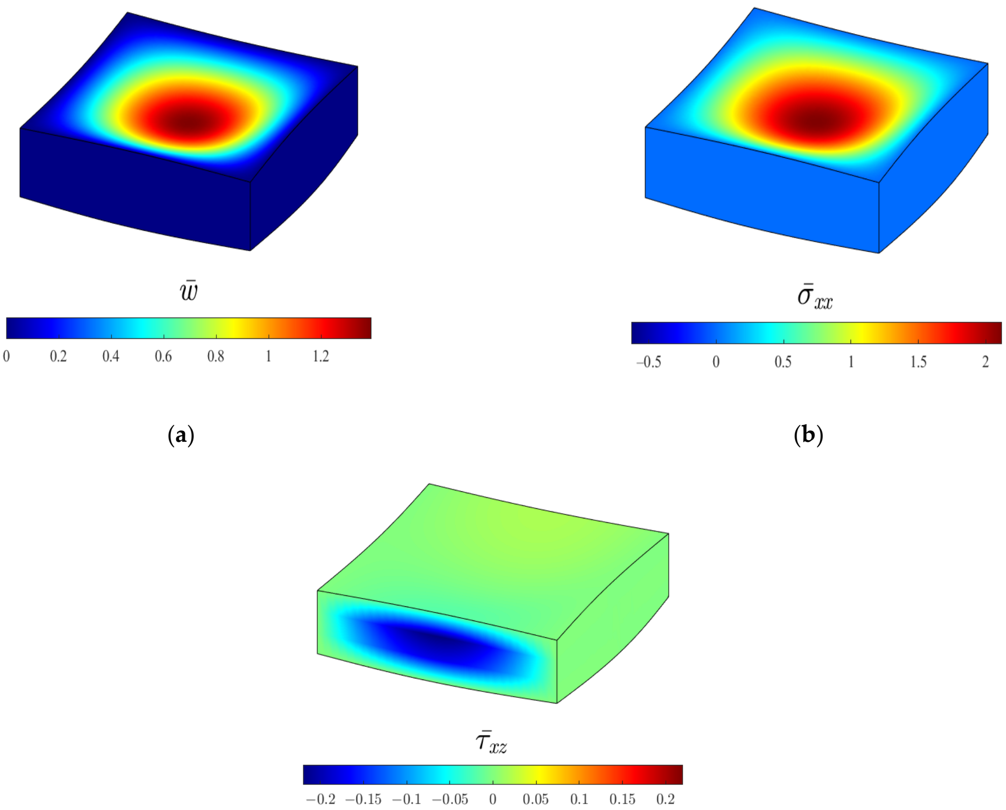

(**a**) (**b**)

(**c**)

Figure 7. Converged 3D responses of Al/Al_2O_3 square plate under a bi-sinusoidal load. (**a**) Three-dimensional responses of $\overline{w}$; (**b**) 3D responses of $\overline{\sigma}_{xx}$; (**c**) 3D responses of $\overline{\tau}_{xz}$.

Table 2. Nondimensional deflection and normal stress of Al/Al_2O_3 square plates with various gradient indexes and aspect ratios.

g	Method	$\overline{w}\left(\frac{a}{2},\frac{a}{2},0\right)$			$\overline{\sigma}_{xx}\left(\frac{a}{2},\frac{a}{2},\frac{h}{3}\right)$		
		$a/h = 4$	$a/h = 10$	$a/h = 100$	$a/h = 4$	$a/h = 10$	$a/h = 100$
1	Quasi-3D [15]	0.7171	0.5875	0.5625	0.6221	1.5064	14.9690
	TSDT-IGA [42]	0.7284	0.5889	0.5625	0.5783	1.4816	14.8890
	FSDT [15]	0.7291	0.5889	0.5625	0.8060	2.0150	20.1500
	Present	0.7172	0.5875	0.5625	0.6219	1.5064	14.9692
4	Quasi-3D [15]	1.1585	0.8821	0.8286	0.4877	1.1971	11.9230
	TSDT-IGA [42]	1.1598	0.8815	0.8287	0.4406	1.1711	11.8436
	FSDT [15]	1.1125	0.8736	0.8286	0.6420	1.6049	16.0490
	Present	1.1589	0.8823	0.8287	0.4884	1.1974	11.9198
10	Quasi-3D [15]	1.3745	1.0072	0.9361	0.3695	0.8965	8.9077
	TSDT-IGA [42]	1.3908	1.0087	0.9362	0.3230	0.8733	8.8582
	FSDT [15]	1.3178	0.9966	0.9360	0.4796	1.1990	11.9900
	Present	1.3757	1.0074	0.9362	0.3657	0.8947	8.9076

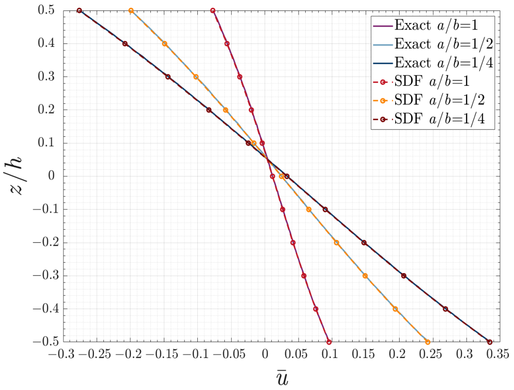

(**a**)

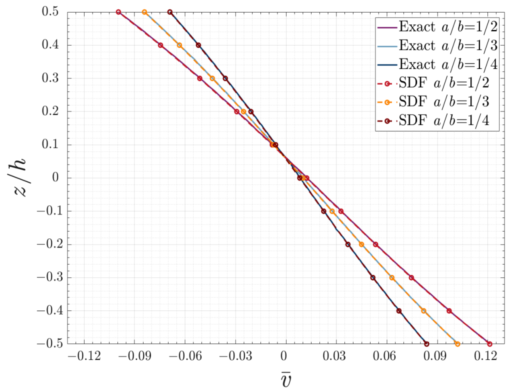

(**b**)

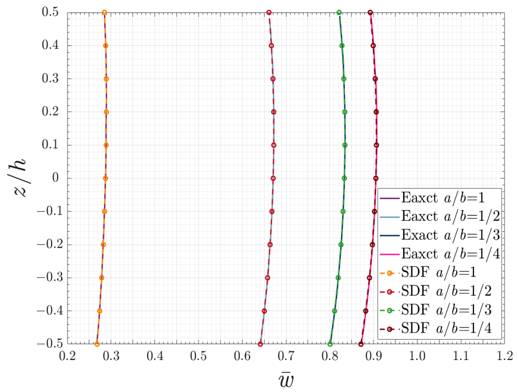

(**c**)

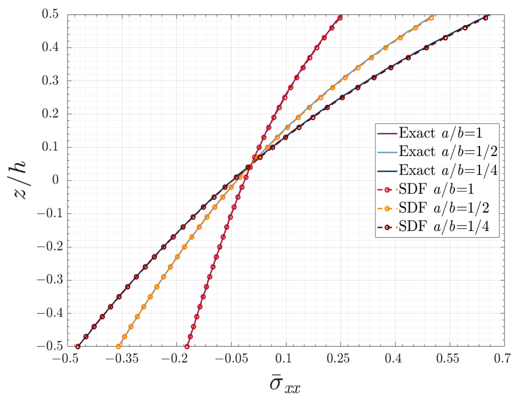

(**d**)

Figure 8. *Cont*.

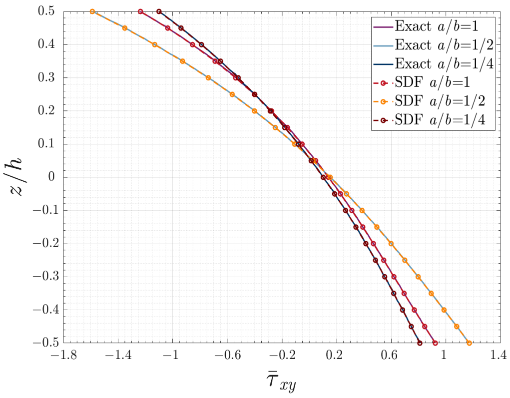

(**e**)

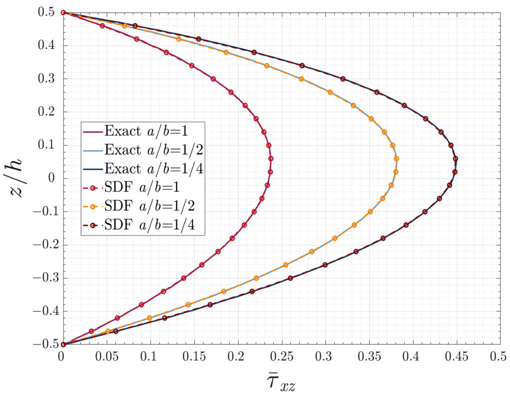

(**f**)

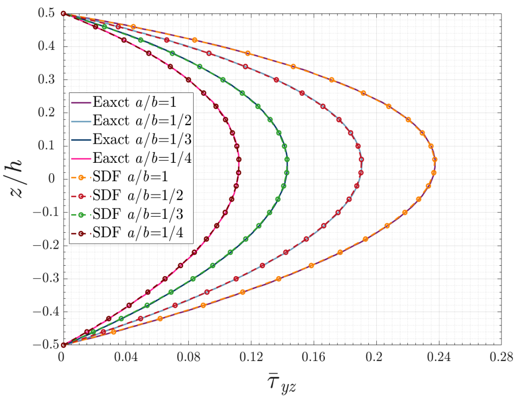

(**g**)

Figure 8. Nondimensional responses through the thickness of E-FGM plates with various width-to-length ratios ($a/h = 4$, $k = 0.5$). (**a**) Variation in $\overline{u}$ through thickness; (**b**) Variation in $\overline{v}$ through thickness; (**c**) Variation of $\overline{w}$ through the thickness; (**d**) Variation in $\overline{\sigma}_{xx}$ through thickness; (**e**) Variation in $\overline{\tau}_{xy}$ through thickness; (**f**) Variation in $\overline{\tau}_{xz}$ through thickness; (**g**) Variation $\overline{\tau}_{yz}$ through thickness.

For further verification, various values of the gradient index k are selected ($a/h = 4$, $b/a = 3$). In Figure 9, the displacement and stress results obtained using the SDF-based IGA method are compared with the exact 3D solutions [16]. It can be observed that the SDF-based IGA results closely match the exact solutions.

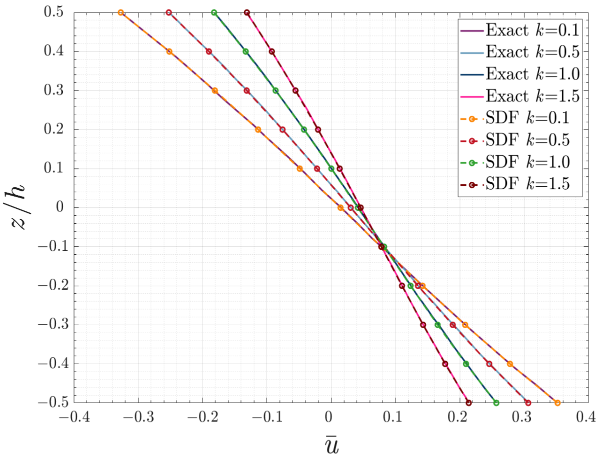

(**a**)

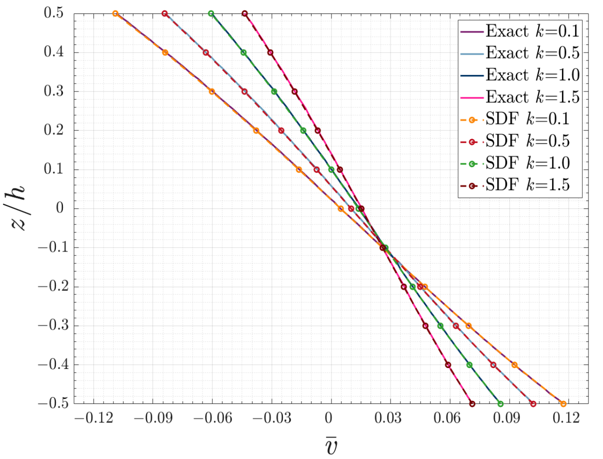

(**b**)

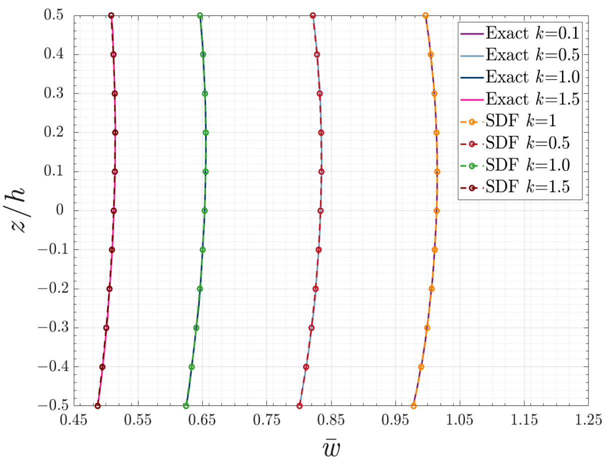

(**c**)

Figure 9. *Cont*.

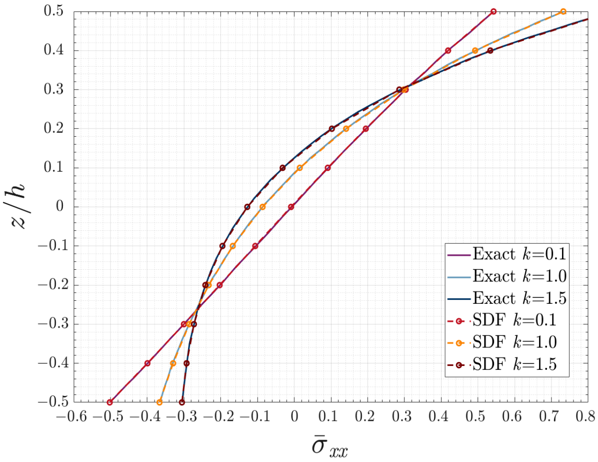

(**d**)

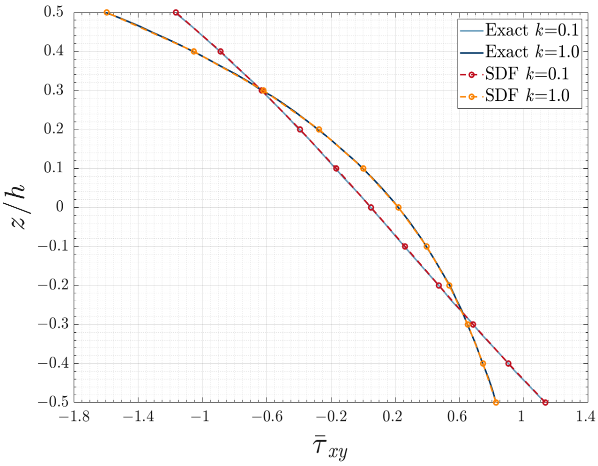

(**e**)

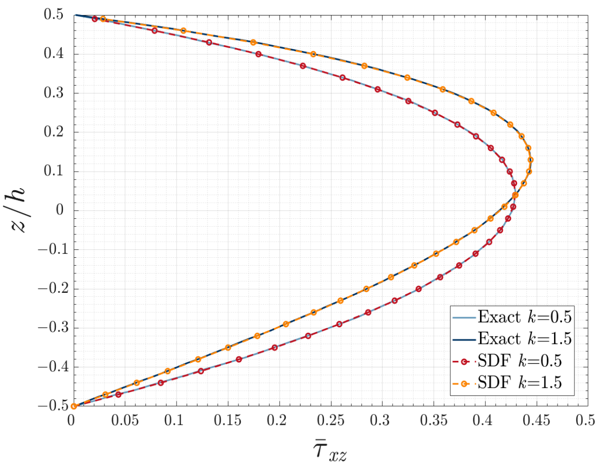

(**f**)

Figure 9. *Cont.*

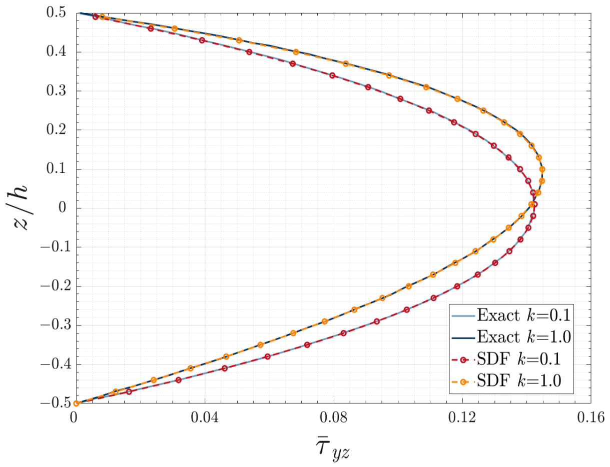

(**g**)

Figure 9. Nondimensional responses through the thickness of an E-FGM plate with various gradient indexes ($a/h = 4$, $b/a = 3$). (**a**) Variation in $\overline{u}$ through thickness; (**b**) Variation in $\overline{v}$ through thickness; (**c**) Variation in $\overline{w}$ through thickness; (**d**) Variation in $\overline{\sigma}_{xx}$ through thickness; (**e**) Variation in $\overline{\tau}_{xy}$ through thickness; (**f**) Variation in $\overline{\tau}_{xz}$ through thickness; (**g**) Variation in $\overline{\tau}_{yz}$ through thickness.

4.3. Circular Ti/ZrO$_2$ Plate

Consider a clamped circular FGM plate made of titanium (Ti) and zirconia (ZrO_2), as depicted in Figure 10. The power law used for comparison purposes is $v_{\mathrm{m}} = (1/2 - z/h)^g$, $v_{\mathrm{c}} = 1 - v_{\mathrm{m}}$, as described in Reddy et al. [51]. The radius, the thickness, and the gradient index are taken as $r = 1$, $h = 0.2$, and $g = 10$, respectively. The top surface of the plate is subjected to a uniform load with amplitude $\varrho_0 = 2 \times 10^9$.

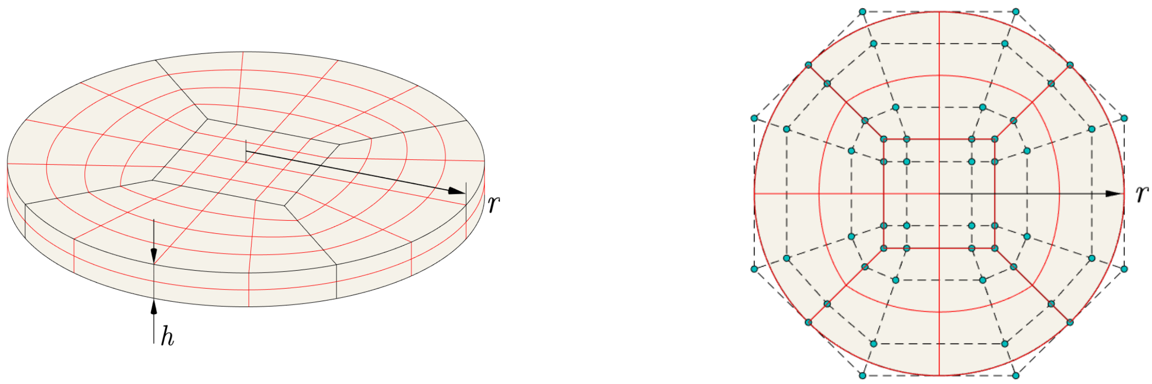

(**a**) (**b**)

Figure 10. Three-dimensional geometry and 2D NURBS midplane of a circular plate. (**a**) Three-dimensional geometry; (**b**) 2D NURBS midplane.

Using fourth-order NURBS basis functions with a 10 × 10 mesh in each patch, taking the SDF truncation numbers $M = 5$, $N = 6$, Figure 11 shows the converged displacement and von Mises stress results. It is seen that the results are continuous and smooth along the interfaces of adjacent patches, which means the patches are well coupled by the penalty method. In addition, a reasonable stress concentration phenomenon is displayed on the boundary of the plate.

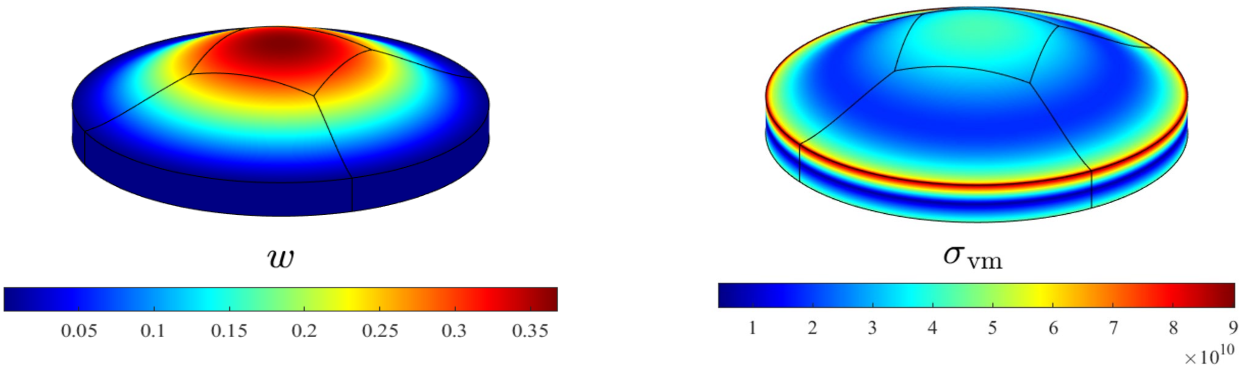

Figure 11. Converged 3D responses of Ti/ZrO_2 circular plate under a uniform load.

The nondimensional deflection is defined as $\overline{w} = \frac{16h^3 E_c}{3r^4 \varrho_0 (1-\nu_c^2)} w$. In Table 3, the central deflection results for various thickness-to-radius ratios and gradient indexes obtained using the SDF-based IGA are compared with the reference solutions in the literature. The reference solutions include FSDT [51], which are analytical solutions based on the FSDT; sFSDT–IGA [52], which are obtained using a simple FSDT with IGA method; and HSDT–IGA [53], which are obtained using Reddy's TSDT with the IGA method. It is seen that the SDF-based IGA results agree well with the HSDT–IGA results, while the FSDT and the sFSDT–IGA are less accurate. Furthermore, as the thickness decreases, the disparity between the results significantly reduces.

Table 3. Nondimensional central deflection $\overline{w}(0,0,0)$ of Ti/ZrO_2 circular plates with various gradient indexes and thickness-to-radius ratios under uni-form load.

h/*r*	Method	*g* = 2	*g* = 4	*g* = 8	*g* = 10	*g* = 50	*g* = 100
0.2	FSDT [51]	1.6130	1.4730	1.3620	1.3330	1.2160	1.1990
	sFSDT–IGA [52]	1.6051	1.4659	1.3548	1.3260	1.2097	1.1918
	HSDT–IGA [53]	1.5958	1.4557	1.3467	1.3187	1.2060	1.1884
	Present	1.5962	1.4556	1.3468	1.3189	1.2065	1.1891
0.1	FSDT [51]	1.4440	1.3200	1.2170	1.1900	1.0800	1.0630
	sFSDT–IGA [52]	1.4428	1.3186	1.2159	1.1889	1.0785	1.0615
	HSDT–IGA [53]	1.4386	1.3143	1.2123	1.1855	1.0762	1.0592
	Present	1.4378	1.3131	1.2112	1.1845	1.0754	1.0620
0.05	FSDT [51]	1.4020	1.2820	1.1810	1.1550	1.0460	1.0290
	sFSDT–IGA [52]	1.4023	1.2817	1.1812	1.1546	1.0458	1.0289
	HSDT–IGA [53]	1.3990	1.2786	1.1785	1.1520	1.0435	1.0267
	Present	1.3990	1.2785	1.1783	1.1518	1.0435	1.0266

4.4. L-Shaped Al/SiC Plate

Consider an L-shaped corner support plate made of aluminum (Al) and silicon carbide (SiC), as shown in Figure 12a. The outer edges of the plate are clamped, and the top surface is subjected to a uniform load of $\varrho_0 = -10^7$. The geometric parameters of the L-shaped plate are defined as $h = 0.2$, $a = 1$, $b = 1.3$, and $r = \phi = 0.3$. In order to achieve a more uniform mesh, 10×10 meshes are used for the 16 NURBS patches, except for the two corner patches B and C, where 15×15 meshes are applied. Fourth-order NURBS basis functions are used, and the SDF truncation numbers are taken as $M = 5$ and $N = 6$.

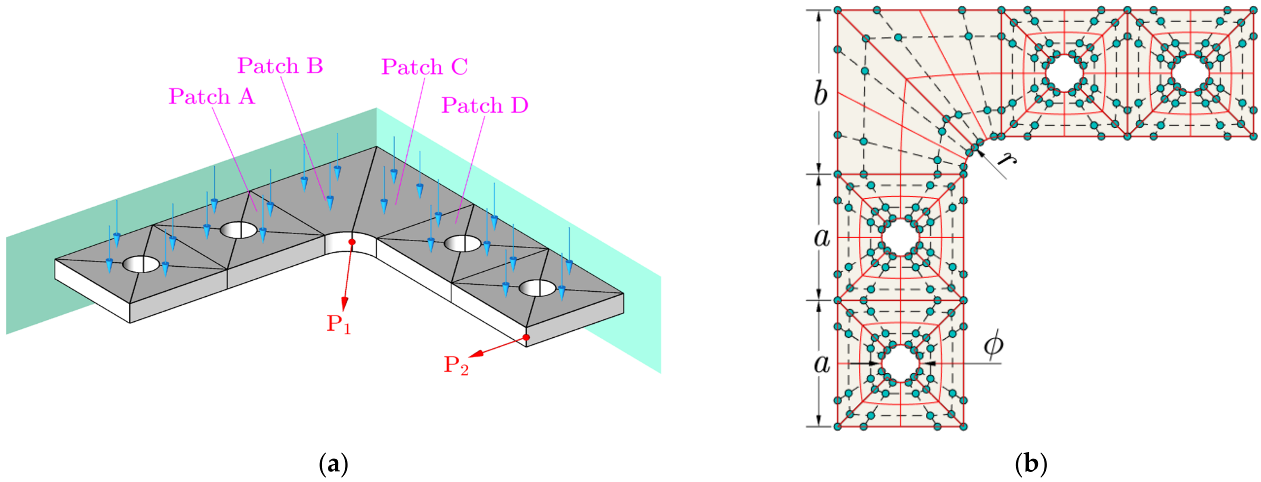

Figure 12. Three-dimensional geometry and 2D NURBS midplane of an L-shaped corner support plate. (**a**) Three-dimensional geometry; (**b**) 2D NURBS midplane.

Taking the gradient index as $g = 4$, Figure 13 shows the displacement and stress results obtained by the SDF-based IGA. The results exhibit good symmetry and smoothness. Reasonable stress concentrations can also be observed near the boundaries.

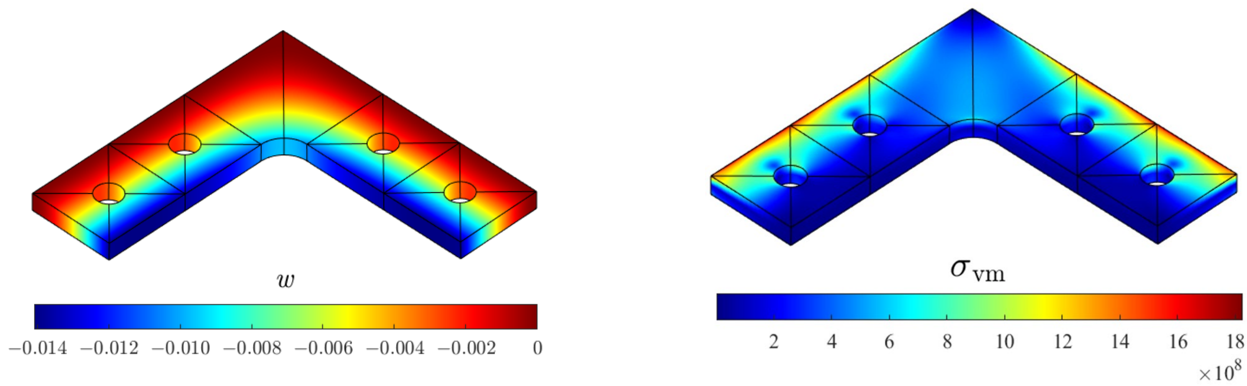

Figure 13. Converged 3D response of Al/SiC L-shaped corner support plate under a uniform load.

In order to verify the accuracy of the SDF-based IGA method for complex geometries, the deflection results from the SDF-based IGA at the points P_1 and P_2 for various thicknesses and gradient indexes are compared with those obtained from the ANSYS, as listed in Table 4. The Ansys results are obtained using Shell181 elements based on the FSDT. In order to approximate the graded material properties, 100 uniform layers are used in the thickness direction. It can be seen that the SDF-based IGA results agree well with the Ansys results, and the discrepancy reduces as the thickness decreases.

Table 4. Deflections at P_1 and P_2 of the Al/SiC L-shaped corner support plate for various gradient indexes and thicknesses.

h	Point	Method	$g = 0$	$g = 2$	$g = 4$	$g = 6$	$g = 8$	$g = 10$
0.2	P_1	Ansys	3.089×10^{-3}	8.246×10^{-3}	9.745×10^{-3}	1.037×10^{-2}	1.083×10^{-2}	1.121×10^{-2}
		Present	3.088×10^{-3}	8.215×10^{-3}	9.714×10^{-3}	1.034×10^{-2}	1.078×10^{-2}	1.117×10^{-2}
	P_2	Ansys	4.480×10^{-3}	1.188×10^{-2}	1.400×10^{-2}	1.488×10^{-2}	1.551×10^{-2}	1.606×10^{-2}
		Present	4.485×10^{-3}	1.183×10^{-2}	1.394×10^{-2}	1.481×10^{-2}	1.544×10^{-2}	1.599×10^{-2}
0.1	P_1	Ansys	2.376×10^{-2}	6.357×10^{-2}	7.431×10^{-2}	7.852×10^{-2}	8.163×10^{-2}	8.442×10^{-2}
		Present	2.464×10^{-2}	6.330×10^{-2}	7.396×10^{-2}	7.813×10^{-2}	8.122×10^{-2}	8.400×10^{-2}
	P_2	Ansys	3.448×10^{-2}	9.166×10^{-2}	1.071×10^{-1}	1.131×10^{-1}	1.176×10^{-1}	1.216×10^{-1}
		Present	3.324×10^{-2}	9.136×10^{-2}	1.067×10^{-1}	1.127×10^{-1}	1.171×10^{-1}	1.212×10^{-1}

5. Conclusions

A novel spectral displacement formulation (SDF) was proposed for analyzing functionally graded material (FGM) plates. This formulation extends the displacements into the Chebyshev series in the thickness direction, resulting in a quasi-3D shear deformation theory with adjustable truncation numbers. By incorporating isogeometric analysis (IGA) for the in-plane discretization, the proposed method can handle FGM plates with complex geometries and various boundary conditions.

Numerical results of the square, rectangular, circular, and L-shaped FGM plates demonstrate the effectiveness of the SDF-based IGA, especially its ability to approach exact 3D elasticity solutions, similar to the well-known Carrera's unified formula (CUF). Compared with the CUF, an important improvement of the SDF is that it is extended from the classical plate theory, which naturally avoids the shear locking problem. This feature makes the SDF-based IGA versatile for analyzing FGM plates of arbitrary thicknesses.

Numerical tests indicate that, for displacement analyses, using SDF truncation numbers $M = 3$ and $N = 3$ is generally enough. However, larger truncation numbers such as $M = 5$ and $N = 6$ are recommended for stress analyses. Of course, the current discussions are limited, and appropriate settings may be changed in different scenarios. Anyhow, the high precision and adjustability of the present method have manifested its great potential in various applications of FGM plates, including strain-based or stress-based reliability analysis, optimization design, thermoelasticity analysis, viscoelasticity analysis, fatigue analysis, and fracture analysis.

Author Contributions: Conceptualization, S.Y., Z.C. and X.S.; methodology, S.Y.; software, S.Y. and X.S.; validation, Y.Z. and Z.C.; formal analysis, S.Y.; writing—original draft preparation, S.Y.; writing—review and editing, S.Y. and X.S.; supervision, Z.C., Y.Z. and H.P. All authors have read and agreed to the published version of the manuscript.

Funding: This research was funded by National Natural Science Foundation of China, grant number U2241263.

Institutional Review Board Statement: Not applicable.

Informed Consent Statement: Not applicable.

Data Availability Statement: Data available on request due to restrictions e.g., privacy or ethical.

Acknowledgments: Thanks to the magazine editors for their careful work, and to the reviewers for their valuable comments.

Conflicts of Interest: The authors declare no conflict of interest.

References

1. Xu, F.; Zhang, X.; Zhang, H. A review on functionally graded structures and materials for energy absorption. *Eng. Struct.* **2018**, *171*, 309–325. [CrossRef]
2. Saleh, B.; Jiang, J.; Fathi, R.; Al-hababi, T.; Xu, Q.; Wang, L.; Song, D.; Ma, A. 30 Years of functionally graded materials: An overview of manufacturing methods, applications and future challenges. *Compos. Part B Eng.* **2020**, *201*, 108376. [CrossRef]
3. Jha, D.K.; Kant, T.; Singh, R.K. A critical review of recent research on functionally graded plates. *Compos. Struct.* **2013**, *96*, 833–849. [CrossRef]
4. Thai, H.T.; Kim, S.E. A review of theories for the modeling and analysis of functionally graded plates and shells. *Compos. Struct.* **2015**, *128*, 70–86. [CrossRef]
5. Swaminathan, K.; Naveenkumar, D.T.; Zenkour, A.M.; Carrera, E. Stress, vibration and buckling analyses of FGM plates—A state-of-the-art review. *Compos. Struct.* **2015**, *120*, 10–31. [CrossRef]
6. Reddy, J.N. A simple higher-order theory for laminated composite plates. *J. Appl. Mech.* **1984**, *51*, 745–752. [CrossRef]
7. Fan, F.; Safaei, B.; Sahmani, . Buckling and postbuckling response of nonlocal strain gradient porous functionally graded micro/nano-plates via NURBS-based isogeometric analysis. *Thin Walled Struct.* **2021**, *159*, 107231. [CrossRef]
8. Nguyen-Xuan, H.; Thai, C.H.; Nguyen-Thoi, T. Isogeometric finite element analysis of composite sandwich plates using a higher order shear deformation theory. *Compos. Part B Eng.* **2013**, *55*, 558–574. [CrossRef]
9. Xiang, S.; Jin, Y.; Bi, Z.; Jiang, S.; Yang, M. A n-order shear deformation theory for free vibration of functionally graded and composite sandwich plates. *Compos. Struct.* **2011**, *93*, 2826–2832. [CrossRef]
10. Touratier, M. An efficient standard plate theory. *Int. J. Eng. Sci.* **1991**, *29*, 901–916. [CrossRef]

11. Soldatos, K.P. A transverse shear deformation theory for homogeneous monoclinic plates. *Acta Mech.* **1992**, *94*, 195–220. [CrossRef]
12. Karama, M.; Afaq, K.S.; Mistou, S. Mechanical behaviour of laminated composite beam by the new multi-layered laminated composite structures model with transverse shear stress continuity. *Int. J. Solids Struct.* **2003**, *40*, 1525–1546. [CrossRef]
13. Mantari, J.L.; Oktem, A.S.; Soares, C.G. A new trigonometric shear deformation theory for isotropic, laminated composite and sandwich plates. *Int. J. Solids Struct.* **2012**, *49*, 43–53. [CrossRef]
14. Hughes, T.J.R.; Cottrell, J.A.; Bazilevs, Y. Isogeometric analysis: CAD, finite elements, NURBS, exact geometry and mesh refinement. *Comput. Methods Appl. Mech. Eng.* **2005**, *194*, 4135–4195. [CrossRef]
15. Carrera, E.; Brischetto, S.; Cinefra, M.; Soave, M. Effects of thickness stretching in functionally graded plates and shells. *Compos. Part B Eng.* **2011**, *42*, 123–133. [CrossRef]
16. Zenkour, A.M. Benchmark trigonometric and 3-D elasticity solutions for an exponentially graded thick rectangular plate. *Arch. Appl. Mech.* **2007**, *77*, 197–214. [CrossRef]
17. Matsunaga, H. Free vibration and stability of functionally graded plates according to a 2-D higher-order deformation theory. *Compos. Struct.* **2008**, *82*, 499–512. [CrossRef]
18. Matsunaga, H. Free vibration and stability of functionally graded shallow shells according to a 2D higher-order deformation theory. *Compos. Struct.* **2008**, *84*, 132–146. [CrossRef]
19. Talha, M.; Singh, B.N. Static response and free vibration analysis of FGM plates using higher order shear deformation theory. *Appl. Math. Model.* **2010**, *34*, 3991–4011. [CrossRef]
20. Mantari, J.L.; Soares, C.G. Generalized hybrid quasi-3D shear deformation theory for the static analysis of advanced composite plates. *Compos. Struct.* **2012**, *94*, 2561–2575. [CrossRef]
21. Mantari, J.L.; Soares, C.G. Optimized sinusoidal higher order shear deformation theory for the analysis of functionally graded plates and shells. *Compos. Part B Eng.* **2014**, *56*, 126–136. [CrossRef]
22. Mantari, J.L.; Soares, C.G. A quasi-3D tangential shear deformation theory with four unknowns for functionally graded plates. *Acta. Mech.* **2015**, *226*, 625–642. [CrossRef]
23. Thai, H.T.; Kim, S.E. A simple quasi-3D sinusoidal shear deformation theory for functionally graded plates. *Compos. Struct.* **2013**, *99*, 172–180. [CrossRef]
24. Thai, H.T.; Vo, T.P.; Bui, T.Q.; Nguyen, T.K. A quasi-3D hyperbolic shear deformation theory for functionally graded plates. *Acta. Mech.* **2014**, *225*, 951–964. [CrossRef]
25. Hebali, H.; Tounsi, A.; Houari, M.S.A.; Bessaim, A.; Bedia, E.A.A. New quasi-3D hyperbolic shear deformation theory for the static and free vibration analysis of functionally graded plates. *J. Eng. Mech.* **2014**, *140*, 374–383. [CrossRef]
26. Bessaim, A.; Houari, M.S.A.; Tounsi, A.; Mahmoud, S.R.; Bedia, E.A.A. A new higher-order shear and normal deformation theory for the static and free vibration analysis of sandwich plates with functionally graded isotropic face sheets. *J. Sandw. Struct. Mater.* **2013**, *15*, 671–703. [CrossRef]
27. Bennoun, M.; Houari, M.S.A.; Tounsi, A. A novel five-variable refined plate theory for vibration analysis of functionally graded sandwich plates. *Mech. Adv. Mater. Struct.* **2016**, *23*, 423–431. [CrossRef]
28. Belabed, Z.; Houari, M.S.A.; Tounsi, A.; Mahmoud, S.R.; Bég, O.A. An efficient and simple higher order shear and normal deformation theory for functionally graded material (FGM) plates. *Compos. Part B Eng.* **2014**, *60*, 274–283. [CrossRef]
29. Mantari, J.L.; Granados, E.V. Thermoelastic analysis of advanced sandwich plates based on a new quasi-3D hybrid type HSDT with 5 unknowns. *Compos. Part B Eng.* **2015**, *69*, 317–334. [CrossRef]
30. Mantari, J.L.; Granados, E.V.; Hinostroza, M.A.; Soares, C.G. Modelling advanced composite plates resting on elastic foundation by using a quasi-3D hybrid type HSDT. *Compos. Struct.* **2014**, *118*, 455–471. [CrossRef]
31. Neves, A.M.A.; Ferreira, A.J.M.; Carrera, E.; Cinefra, M.; Roque, C.M.C.; Jorge, R.M.N.; Soares, C.M.M. A quasi-3D hyperbolic shear deformation theory for the static and free vibration analysis of functionally graded plates. *Compos. Struct.* **2012**, *94*, 1814–1825. [CrossRef]
32. Neves, A.M.A.; Ferreira, A.J.M.; Carrera, E.; Cinefra, M.; Jorge, R.M.N.; Soares, C.M.M. Buckling analysis of sandwich plates with functionally graded skins using a new quasi-3D hyperbolic sine shear deformation theory and collocation with radial basis functions. *ZAMM J. Appl. Math. Mech.* **2012**, *92*, 749–766. [CrossRef]
33. Mantari, J.L.; Oktem, A.S.; Soares, C.G. A new higher order shear deformation theory for sandwich and composite laminated plates. *Compos. Part B Eng.* **2012**, *43*, 1489–1499. [CrossRef]
34. Farzam-Rad, S.A.; Hassani, S.A.B.; Karamodin, A. Isogeometric analysis of functionally graded plates using a new quasi-3D shear deformation theory based on physical neutral surface. *Compos. Part B Eng.* **2017**, *108*, 74–189. [CrossRef]
35. Sun, X.; Gao, R.; Zhang, Y. Spectral stochastic isogeometric analysis of bending and free vibration of porous functionally graded plates. *Appl. Math. Model.* **2023**, *116*, 711–734. [CrossRef]
36. Neves, A.M.A.; Ferreira, A.J.M.; Carrera, E.; Cinefra, M.; Roque, C.M.C.; Jorge, R.M.N.; Soares, C.M.M. Static, Free vibration and buckling analysis of isotropic and sandwich functionally graded plates using a quasi-3D higher-order shear deformation theory and a meshless technique. *Compos. Part B Eng.* **2013**, *44*, 657–674. [CrossRef]
37. Montassir, S.; Moustabchir, H.; Elkhalfi, A. Application of NURBS in the Fracture Mechanics Framework to Study the Stress Intensity Factor. *Stat. Optim. Inf. Comput.* **2023**, *11*, 106–115.
38. Yakoubi, K.; Montassir, S.; Moustabchir, H.; Elkhalfi, A.; Scutaru, M.L.; Vlase, S. T-Stress Evaluation Based Cracking of Pipes Using an Extended Isogeometric Analysis (X-IGA). *Symmetry* **2022**, *14*, 1065. [CrossRef]

39. Bao, G.; Wang, L. Multiple cracking in functionally graded ceramic/metal coatings. *Int. J. Solids Struct.* **1995**, *32*, 2853–2871. [CrossRef]
40. Szilard, R. Theories and applications of plate analysis: Classical, numerical and engineering methods. *Appl. Mech. Rev.* **2004**, *57*, B32–B33. [CrossRef]
41. Boyd, J.P. *Chebyshev and Fourier Spectral Methods*; Courier Corporation: Chelmsford, MA, USA, 2001; pp. 101–105.
42. Thai, C.H.; Kulasegaram, S.; Tran, L.V.; Nguyen-Xuan, H. Generalized shear deformation theory for functionally graded isotropic and sandwich plates based on isogeometric approach. *Comput. Struct.* **2014**, *141*, 94–112. [CrossRef]
43. Nguyen, T.N.; Thai, C.H.; Nguyen-Xuan, H.; Lee, J. Geometrically nonlinear analysis of functionally graded material plates using an improved moving Kriging meshfree method based on a refined plate theory. *Compos. Struct.* **2018**, *193*, 268–280. [CrossRef]
44. Cottrell, J.A.; Hughes, T.J.R.; Bazilevs, Y. *Isogeometric Analysis: Toward Integration of CAD and FEA*; John Wiley and Sons: Hoboken, NJ, USA, 2009; pp. 154–176.
45. Piegl, L.; Tiller, W. *The NURBS Book*; Springer Science and Business Media: Berlin, Germany, 2012; pp. 1–254.
46. Farin, G. *Curves and Surfaces for Computer-Aided Geometric Design: A Practical Guide*; Elsevier: Cham, Switzerland, 2014; pp. 154–296.
47. Brannon, R.M. *Curvilinear Analysis in a Euclidian Space*; University of New Mexico: Albuquerque, NM, USA, 2004; pp. 78–97.
48. Adam, C.; Hughes, T.J.R.; Bouabdallah, S.; Zarroug, M.; Maitournam, H. Selective and reduced numerical integrations for NURBS-based isogeometric analysis. *Comput. Methods Appl. Mech. Eng.* **2015**, *284*, 732–761. [CrossRef]
49. Zienkiewicz, O.C.; Xu, Z.; Zeng, L.F.; Samuelsson, A.; Wiberg, N.E. Linked interpolation for Reissner-Mindlin plate elements: Part I—A simple quadrilateral. *Int. J. Numer. Methods Eng.* **1993**, *36*, 3043–3056. [CrossRef]
50. Nguyen, N.D.; Nguyen, T.K.; Nguyen, T.N.; Thai, H.T. New Ritz-solution shape functions for analysis of thermo-mechanical buckling and vibration of laminated composite beams. *Compos. Struct.* **2018**, *184*, 452–460. [CrossRef]
51. Reddy, J.N.; Wang, C.M.; Kitipornchai, S. Axisymmetric bending of functionally graded circular and annular plates. *Eur. J. Mech. A/Solids* **1999**, *18*, 185–199. [CrossRef]
52. Yin, S.; Hale, J.S.; Yu, T.; Bui, T.Q.; Bordas, S.P. Isogeometric locking-free plate element: A simple first order shear deformation theory for functionally graded plates. *Compos. Struct.* **2014**, *118*, 121–138. [CrossRef]
53. Tran, L.V.; Ferreira, A.J.M.; Nguyen, X.H. Isogeometric analysis of functionally graded plates using higher-order shear deformation theory. *Compos. Part B Eng.* **2013**, *51*, 368–383. [CrossRef]